Nuclear Instruments and Methods in Physics Research A 610 (2009) 488–501

Contents lists available at ScienceDirect

Nuclear Instruments and Methods in Physics Research A

journal homepage: www.elsevier.com/locate/nima

Dual-readout calorimetry with a full-size BGO electromagnetic section

N. Akchurin [a], F. Bedeschi [b], A. Cardini [c], R. Carosi [b], G. Ciapetti [d], R. Ferrari [e], S. Franchino [f], M. Fraternali [f], G. Gaudio [e], J. Hauptman [g], M. Incagli [b], F. Lacava [d], L. La Rotonda [h], T. Libeiro [a], M. Livan [f], E. Meoni [h], D. Pinci [d], A. Policicchio [h,1], S. Popescu [a], F. Scuri [b], A. Sill [a], W. Vandelli [i], T. Venturelli [h], C. Voena [d], I. Volobouev [a], R. Wigmans [a,*]

[a] Texas Tech University, Lubbock, TX, USA
[b] Dipartimento di Fisica, Università di Pisa and INFN Sezione di Pisa, Italy
[c] Dipartimento di Fisica, Università di Cagliari and INFN Sezione di Cagliari, Italy
[d] Dipartimento di Fisica, Università di Roma "La Sapienza" and INFN Sezione di Roma, Italy
[e] INFN Sezione di Pavia, Italy
[f] INFN Sezione di Pavia and Dipartimento di Fisica Nucleare e Teorica, Università di Pavia, Italy
[g] Iowa State University, Ames, IA, USA
[h] Dipartimento di Fisica, Università della Calabria and INFN Cosenza, Italy
[i] CERN, Genève, Switzerland

ARTICLE INFO

Article history:
Received 9 April 2009
Received in revised form
29 June 2009
Accepted 5 August 2009
Available online 6 September 2009

Keywords:
Calorimetry
Cherenkov light
Crystals
Optical fibers

ABSTRACT

Beam tests of a hybrid dual-readout calorimeter are described. The electromagnetic section of this instrument consists of 100 BGO crystals and the hadronic section is made of copper in which two types of optical fibers are embedded. The electromagnetic fraction of hadronic showers developing in this calorimeter system is estimated event by event from the relative amounts of Cherenkov light and scintillation light produced in the shower development. The benefits and limitations of this detector system for the detection of showers induced by single hadrons and by multiparticle jets are investigated. Effects of side leakage on the detector performance are also studied.

1. Introduction

In recent years, dual-readout calorimetry has emerged as a promising new solution for the need to detect both leptons and hadrons with excellent precision in high-energy particle physics experiments [1]. The Dual Readout Method (DREAM) is based on a simultaneous measurement of different types of signals which provide complementary information about details of the shower development. It has been argued [2,3] and experimentally demonstrated [4] that a comparison of the signals produced by Cherenkov light and scintillation light makes it possible to measure the energy fraction carried by the electromagnetic shower component, f_{em}, event by event. Since fluctuations in f_{em} are responsible for all traditional problems in calorimetric hadron detection, this may lead to an important improvement in the performance of hadron calorimeters [5].

The first calorimeter of this type was based on a copper absorber structure, equipped with two types of active media. In this detector, scintillating fibers measured the total energy deposited by the shower particles, while Cherenkov light, generated by the charged, relativistic shower particles, was produced in undoped optical fibers [4,6]. It was recently demonstrated that the signals from certain high-density crystals ($PbWO_4$, BGO) can also be unraveled into Cherenkov and scintillation components [7], and that such crystals, when used in conjunction with the fiber calorimeter mentioned above, offer in principle the same advantages for hadronic shower detection as the latter [8].

In this paper, we describe high-energy beam tests of a hybrid calorimeter system that consisted of a full-size electromagnetic section made of BGO crystals, backed up by a dual-readout fiber hadronic section, and surrounded by a system of lateral leakage counters. In Section 2, the detectors and the experimental setup in which they were tested are described. In Section 3, we discuss the experimental data that were taken and the methods used to analyze these data. The experimental results are presented in Section 4, and conclusions are given in Section 5.

* Corresponding author. Fax: +1 806 742 1182.
E-mail address: wigmans@ttu.edu (R. Wigmans).
[1] Now at Department of Physics, University of Washington, Seattle, WA, USA.

0168-9002/$ - see front matter © 2009 Elsevier B.V. All rights reserved.
doi:10.1016/j.nima.2009.08.074

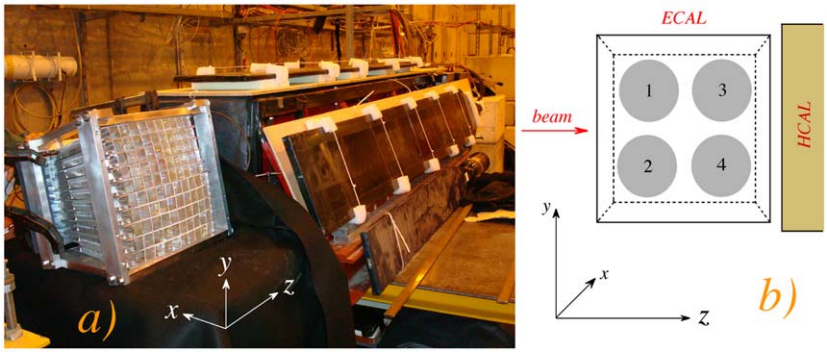

Fig. 1. The calorimeter during installation in the H4 test beam, which runs from the bottom left corner to the top right corner in this picture. The 100-crystal BGO matrix is located upstream of the fiber calorimeter, and is read out by four PMTs on the left (small end face) side. Some of the leakage counters are visible as well (a). The location and numbering of the PMTs reading out the BGO crystal matrix (b).

2. Detectors and experimental setup

2.1. Detectors and readout

The calorimeter system used in these experiments consisted of two sections. The electromagnetic section (ECAL) consisted of 100 crystals of bismuth germanate ($Bi_4Ge_3O_{12}$, or BGO), and the hadronic section (HCAL) was the original DREAM fiber calorimeter [4].

The BGO crystals were 24 cm long and tapered. One end face had a cross-section of $2.4 \times 2.4\,cm^2$, the other one measured $3.2 \times 3.2\,cm^2$. These BGO crystals were previously used in the electromagnetic calorimeter of the L3 experiment [9]. The 100 crystals used for our tests formed a projective segment from this calorimeter. This segment was placed perpendicular to the beam line, as illustrated in Fig. 1. For particles entering the calorimeter in its geometrical center, the ECAL thus had an effective thickness of 28 cm, which corresponds to 25 radiation lengths (X_0) or 1.3 nuclear interaction lengths (λ_{int}).

For the purpose of these tests, this ensemble of crystals was considered one unit. The PMTs were specially selected for this application, for which we needed a light detector that was fast, had a large surface area and a low gain. This unusual combination of properties was found in XP4362B,[2] a 6-stage PMT (nominal gain 10^4) with a 3-in. active surface area and a nominal rise time of 2.0 ns. Four such PMTs were facing the small end face side of the crystals. The distance between the PMT photocathodes and the crystal surface was about 5 cm. Each PMT thus detected light produced in at least 10 different crystals.

It should be emphasized that this readout arrangement was in many ways far from ideal. It was necessitated by the fact that, in order to split the BGO signals into Cherenkov and scintillation components, the time structure of each BGO signal needed to be measured in great detail. We had only four electronic channels available for this purpose (see Section 2.3). Therefore, we chose to detect this light with four large PMTs, each covering some fraction of the crystals. This setup had of course several major drawbacks:

(1) No optical contact between the crystals and the photocathodes. Because of the large index of refraction ($n = 2.15$), this resulted in large light losses.
(2) Sensitivity to quantum efficiency variations over the photocathode surfaces. This translated directly into large response non-uniformities, since the signal depended on the crystal in which the light was produced.
(3) A strong left–right dependence of the calorimeter response, as a result of the tapered shape of the crystals. Because of internal reflection, light produced in the right half of the crystal had a much smaller detection probability than light produced near the small exit face.
(4) Insensitivity to light produced in the peripheral regions of the matrix, which were not covered at all by these four PMTs.

However, our goal in these tests was *not* to set new performance records for calorimeters, but rather to demonstrate that the dual-readout principles also work in a hybrid calorimeter system when, on average, a large fraction of the energy is deposited in the homogeneous detector section. In view of this limited goal, this improvised readout scheme turned out to be adequate.

The basic element of the hadronic DREAM calorimeter section was an extruded copper rod, 2 m long and $4 \times 4\,mm^2$ in cross-section. This rod was hollow, and the central cylinder had a diameter of 2.5 mm. Seven optical fibers were inserted in this hole. Three of these were plastic scintillating fibers, the other four fibers were undoped, intended for detecting Cherenkov light. The instrumented volume had a length of 2.0 m ($10\lambda_{int}$, $100X_0$), an effective radius of 16.2 cm and a mass of 1030 kg. The fibers were grouped to form 19 hexagonal towers. The effective radius of each tower was 37.1 mm ($1.82R_M$). A central tower was surrounded by two hexagonal rings. The towers were longitudinally unsegmented. The fibers sticking out at the rear end of this structure were separated into 38 bunches: 19 bunches of scintillating fibers and 19 bunches of Cherenkov fibers. In this way, the readout structure was established. Each bunch was coupled through a 2 mm air gap to a PMT.[3] More information about this detector, and its performance in stand-alone mode, is given elsewhere [4,6].

Despite its mass of more than one metric ton, hadronic showers developing in this structure were not fully contained. We have shown in an earlier paper [10] that, on average, $\sim 10\%$ of the energy carried by a 100 GeV hadron leaks out, most of it sideways, in the absorption process in this calorimeter. Event-to-event fluctuations about this average turned out to be the dominating factor limiting the hadronic energy resolution of the DREAM calorimeter, after fluctuations in the em shower fraction were successfully eliminated.

Of course, the ideal way for dealing with these leakage fluctuations would be to build a sufficiently large detector. Measurements of the shower profiles indicated that the mass had to be increased by a factor of five to limit the contribution of leakage fluctuations to the hadronic energy resolution to 1% [10]. An alternative method, which fit within our budget, is to surround

[2] Manufactured by Photonis, France.

[3] Hamamatsu R580, 10-stage, ∅ 38 mm, bialkali photocathode, borosilicate window.

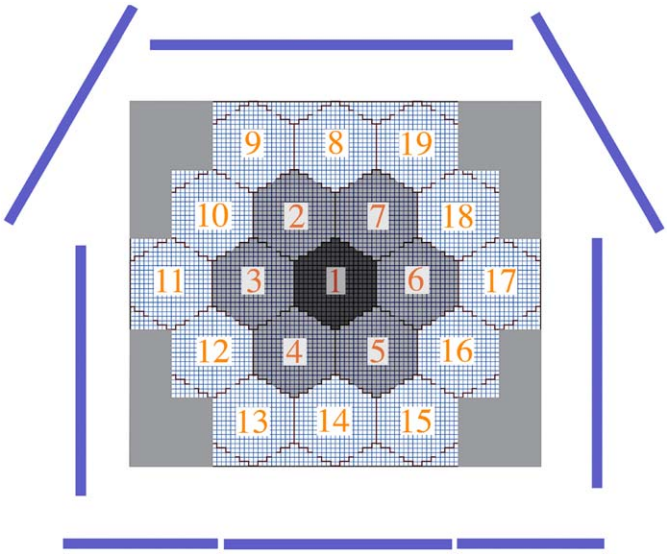

Fig. 2. Transverse cross-section of the DREAM fiber calorimeter, surrounded by the eight leakage counters. The tower numbering corresponds to the front view of the detector.

the calorimeter with large scintillator paddles, and use the signals in these detectors as a measure for the energy leakage. This was the approach chosen in the tests described in this paper. We used in total eight scintillator paddles, with lengths up to 2 m, a thickness of 1 cm, and widths varying from 15 to 30 cm, which formed a cylinder surrounding the DREAM calorimeter (see Fig. 2).

2.2. Experimental setup

All measurements described in this paper were performed in the H4 beam line of the Super Proton Synchrotron at CERN. The calorimeters were mounted on a platform that could move vertically and sideways with respect to the beam. Two small scintillation counters (TC) provided the signals that were used to trigger the data acquisition system. These trigger counters were 2.5 mm thick, and the area of overlap was $6\times 6\,\mathrm{cm}^2$. A coincidence between the logic signals from these counters provided the trigger. The trajectories of individual beam particles could be reconstructed with the information provided by two small drift chambers (DC). One of these was installed upstream of the trigger counters, the other one downstream. These drift chambers made it possible to determine the location of the impact point of the beam particles at the calorimeter with a precision of typically ~ 0.2 mm. Ten meters downstream of the calorimeters, behind an additional $6\lambda_{\mathrm{int}}$ of absorber material, a large ($84\times 34\times 2.0\,\mathrm{cm}^3$) scintillation counter served to identify beam muons and/or muons generated in hadronic shower development upstream. The experimental setup is schematically depicted in Fig. 3.

Modern experiments in particle physics focus on the detection of *jets*, rather than on individual hadrons. From the perspective of the calorimeter system, a jet is, in good approximation, a collection of photons and pions, which develop simultaneous showers in the same detector volume. In order to study the detector performance for such multiparticle events, we installed a 10 cm thick polyethylene target ($\sim 0.1\lambda_{\mathrm{int}}$) in front of the calorimeter system. Additional scintillation counters were placed directly upstream and downstream of this target. With this setup, nuclear interactions of beam pions in the target could be selected, by requiring a mip signal in the upstream counter (indicating the passage of a single pion) and a much larger signal in the downstream counter (ITC). The events selected in this way are of course not representative of typical jets (i.e., fragmenting quarks or gluons) studied in modern high-energy colliding-beam experiments. However, for purposes of calorimetry they were nevertheless useful, since they exhibited the main characteristic that makes jet detection with a calorimeter system different from the mono-energetic hadrons provided by the accelerator: a varying number of particles with unknown energy and unknown composition, which developed simultaneous showers in the calorimeter system. And since the *total energy* of this particle collection was approximately known (apart from some losses in the target, and secondaries produced at such large angles that they missed the calorimeter), some indication of the jet energy resolution could be derived from these measurements.

2.3. Data acquisition

Measurement of the time structure of the (crystal) calorimeter signals formed a very important part of the tests described here. In order to limit distortion of this structure as much as possible, we used special 15 mm thick cables to transport the crystal signals to the counting room. Such cables were also used for the signals from the trigger counters, and these were routed such as to minimize delays in the DAQ system.[4] The HCAL signals were transported through RG-58 cables with (for timing purposes) appropriate lengths to the counting room.

The data acquisition system used VME electronics. A single VME crate hosted all the needed readout and control boards. The charge measurements of the signals from the DREAM towers, the leakage counters and the muon counter were performed with two CAEN V792AC QADC 32-channel modules,[5] each channel offering 12-bit digitization at a sensitivity of 100 fC/count and a conversion time below 10 μs. The timing information of the tracking chambers was recorded with 1 ns resolution in a 16-bit 16-channel LeCroy 1176 TDC.[6]

The time structure of the ECAL signals was recorded by means of a Tektronix TDS 7254B digital oscilloscope,[7] which provided a sampling capability of 5 GSample/s, at an analog bandwidth of 2.5 GHz, over four input channels. We sampled the signals from the four PMTs that detected the light generated in the BGO crystal matrix at a rate of 1.25 GHz, i.e., at 0.8 ns intervals. The oscilloscope gain (scale) was tuned in order to optimize the exploitation of the 8-bit dynamic range for each beam energy, maintaining both a good sensitivity and a small fraction of overflow events. The BGO signals were followed over a time interval of 224 ns, during which time 282 amplitude measurements were performed. As is shown in Section 3, these measurements made it possible to distinguish the contributions from Cherenkov and scintillation light to the signals with excellent precision.

The trigger logic was implemented through NIM modules and the signals sent to a VME I/O register, which was also receiving the spill and the global busy information. Moreover, the system was able to inject pedestal triggers during the data taking, enabling the parallel recording of pedestal data. Pedestal events were flagged with a special signal on the VME I/O register. The VME crate was linked to a data acquisition computer through an SBS 620 optical VME-PCI interface[8] which allowed memory mapping

[4] We measured the signal speed to be 0.78*c* in these cables.
[5] http://www.caen.it/nuclear/Printable/data_sheet.php?mod=V792&fam=vme&fun=qdc
[6] http://www.lecroy.com/lrs/dsheets/1176.htm
[7] http://www.tek.com/site/ps/0,,55-13766-SPECS_EN,00.html
[8] http://www.gefanucembedded.com/products/457

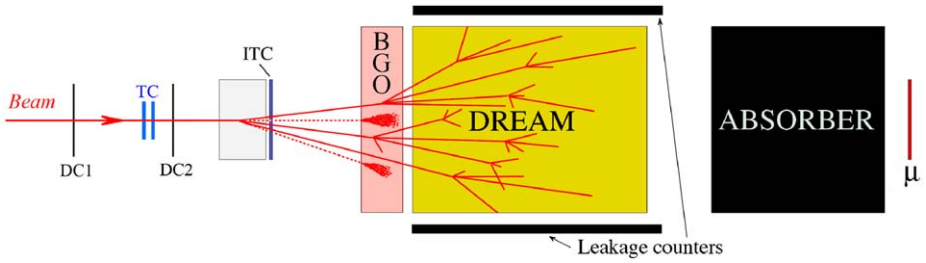

Fig. 3. Schematic of the experimental setup in the beam line in which the hybrid calorimeter system was tested (see text for details). Also shown is the occurrence and development of a multi-particle event ("jet") originating in the upstream target.

of the VME resources via an open source driver.[9] The computer was equipped with a Pentium-4 2 GHz CPU, 1 GB of RAM, and running a CERN SLC 4.3 operating system.[10]

The data acquisition was built around a single-event polling mechanism and performed by a readout program that was streaming physics and on-spill pedestal events into two independent first-in-first-out buffers, built on top of 32 MB shared memories. Two recorder programs were then dumping the data from the shared memories to the disk. Only exclusive accesses to shared buffers were allowed and concurrent requests were synchronized with semaphores. This scheme optimized the CPU utilization and increased the data taking efficiency thanks to the bunch structure of the SPS cycle, where beam particles were provided to our experiment during a spill of 9.6 s, with a repetition period of 48 s.

On the other hand, due to the large oscilloscope data size and its poor on-line performance, we decided to handle that on a multi-event basis. Through the GPIB interface, the scope was prepared to acquire events before the extraction and delivery of protons on target. On spill, all events were sequentially recorded in the internal memory of the scope. At the end of the spill, the oscilloscope memory was dumped over a temporary file, in a network-mounted shared disk. At this point, the file was read out and the data copied in properly formatted areas in the shared-memory buffers, where the information from all the VME modules had already been stored, in real time, by the readout program. In sequence, the recorder programs were then dumping the events to disk and a monitoring program was running in spy mode, on top of the physics shared memory, producing online histograms.

With this scheme, we were able to reach, in spill, a data acquisition rate of ~ 2 kHz, limited by the size of the internal scope buffer. Since no pedestal suppression was implemented, the data volume was proportional to this rate, and amounted, at maximum, to ~ 1.5 MB/spill, largely dominated by the oscilloscope data.

2.4. Calibration of the detectors

The PMTs reading out the signals from the eight leakage counters and the muon counter were calibrated with 150 GeV muons (μ^+). For this purpose, the leakage counters were lined up behind the calorimeters and placed perpendicular to the (muon) beam line. For each of the nine counters, the high-voltage was chosen such that the most probable value of the (Landau) signal distribution corresponded to about 50 ADC counts above pedestal. The average signal generated by the muons while traversing a counter perpendicularly will be referred to as a *mip*. All nine counters were calibrated in terms of *mip* s, i.e., for each counter the calibration constant was defined as the number of *mip* s per ADC count.

[9] http://www.awa.tohoku.ac.jp/~sanshiro/kinoko-e/vmedrv/
[10] http://linux.web.cern.ch/linux/scientific4/

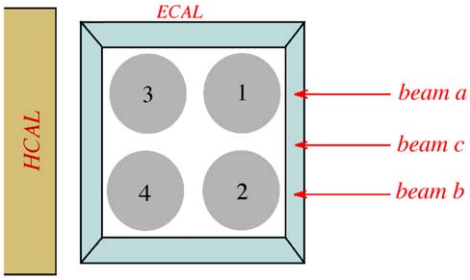

Fig. 4. Side view of the calorimeter system. The PMTs reading out the crystal matrix are represented by the gray circles. The beam positions used for calibrating these PMTs are indicated by arrows.

All PMTs reading out the calorimeter signals were calibrated with 50 GeV electrons. For the calibration of the 38 channels of the HCAL (19 scintillation and 19 Cherenkov, see Fig. 2), the ECAL was moved out of the beam line, so that these electrons could deposit all their energy in the exposed HCAL towers. The showers generated by these particles were not completely contained in a single HCAL tower. The (average) containment was found from EGS4 Monte Carlo simulations [11]. When the electrons entered a tower in its geometrical center, on average 92.5% of the scintillation light and 93.6% of the Cherenkov light was generated in that tower [6]. The remaining fraction of the light was shared by the surrounding towers. The signals observed in the exposed tower thus corresponded to an energy deposit of 46.3 GeV in the case of the scintillating fibers and of 46.8 GeV for the Cherenkov fibers. The mentioned energies, together with the precisely measured values of the average signals from the exposed calorimeter towers, formed the basis for determining the calibration constants, i.e., the relationship between the measured number of ADC counts and the corresponding energy deposit (GeVs per ADC count).

The most complicated aspect of the detector calibration concerned the four PMTs that detected the signals from the BGO crystal matrix (Fig. 4). The problems derived from the fact that the response of an individual PMT depended on the impact point of the particles. Moreover, each PMT only detected part of the shower developed by a 50 GeV electron in the crystal matrix: PMTs 1 and 2 detected the early part of the shower development, PMTs 3 and 4 detected light generated in the late stages. The calibration was performed as follows.

Defining the calibration constants for the four PMTs as a_m (with $m = 1, \ldots, 4$), and the signals from these PMTs for the i th event as $B_{m,i}$, the total BGO signal for that event, S_i, is given by

$$S_i = \sum_{m=1}^{4} a_m B_m$$

and this should be, on average, equal to the beam energy, E_n, for each run (n). The expected rms value of the fluctuations in this sum is $\sigma_n \propto 1/\sqrt{E_n}$, so $\sigma_n^2 \propto E_n^{-1}$.

A chi-squared that imposes optimum linearity (but not optimum resolution) is

$$\chi^2 = \sum_n \sum_i \left\{ \frac{E_n - \sum_m a_m B_{m,i}}{\sigma_n} \right\}^2 .$$

By setting partial derivatives to zero,

$$0 = \frac{\partial \chi^2}{\partial a_k} = -2 \sum_n \sum_i \frac{E_n - \sum_m a_m B_{m,i}}{\sigma_n^2} \cdot B_{k,i} \quad (k = 1, \ldots, 4)$$

and, arranging terms into a set of linear equations in a_m,

$$\sum_n \sum_i \frac{E_n B_{k,i}}{\sigma_n^2} = \sum_m a_m \sum_n \sum_i \frac{B_{m,i} B_{k,i}}{\sigma_n^2}$$

we obtain a set of linear equations $c_k = \sum_m a_m M_{m,k}$,

with $c_k = \sum_n \sum_i \frac{E_n B_{k,i}}{\sigma_n^2}$ and $M_{m,k} = \sum_n \sum_i \frac{B_{m,i} B_{k,i}}{\sigma_n^2}$.

The solution for the constants a_k is $\vec{a} = M^{-1}\vec{c}$.

We used a large variety of electron data for this calibration. Beams with energies of 10, 20, 30, 50, 100, 150 and 200 GeV were steered into each of the points *a*, *b* and *c* indicated in Fig. 4. The calibration constants were derived from all the data collected in these 21 different runs.

The signals $B_{m,i}$ used in this procedure represented the integrated charge collected in the first 115 ns after the start of the BGO signals. They were thus expressed in units of [mV ns]. The four constants a_k derived from this procedure all share the same relationship between an energy unit and 1 mV ns; they are *intercalibrated*.

However, in order to determine the final calibration constants (expressed in GeVs per millivolt-nanosecond), the BGO signals first had to be unraveled into their scintillation and Cherenkov components. This procedure is described in Section 3.2, where we also finalize the description of the calibration procedure for these separate signals.

3. Experimental data and methods

3.1. Experimental data

Most of the measurements described in this paper were performed with pion beams. Negatively charged pions of 20 and 50 GeV, and π^+ beams of 100, 150, 200 and 300 GeV were steered into each of the positions *a*, *b* and *c* indicated in Fig. 4. In each run, 50 000 events were recorded. In addition, multiparticle "jets" of 100, 200 and 300 GeV were created with π^+ beams steered into the center of the calorimeter system. The polyethylene target (see Section 2.2) was placed 35 cm upstream of the ECAL for these measurements, and we selected interactions with a minimum multiplicity of 10 by means of a threshold on the signals from the ITC counter downstream of this target. At each energy, 200 000 events were collected this way. In order to investigate possible biases, we also collected 50 000 events without such a threshold, for each energy. The pion beams contained some muons, at the few-% level. These muons were easily recognized (using the muon counter) and removed from the event samples.

In order to study the performance of the BGO crystal matrix in this unusual geometry, we used electron beams with energies of 10, 20, 30, 50,100, 150 and 200 GeV.

3.2. Exploiting the BGO signals

BGO is a bright scintillator, Cherenkov radiation represents only a tiny fraction of the light generated by high-energy particle showers. Yet, the very different optical spectra and time structures offer good possibilities for distinguishing between these two components. In a previous paper, we have demonstrated that an ultraviolet filter, combined with a detailed measurement of the time structure makes it possible to measure the contributions of scintillation and Cherenkov light to the crystal signals event by event with excellent precision [7].

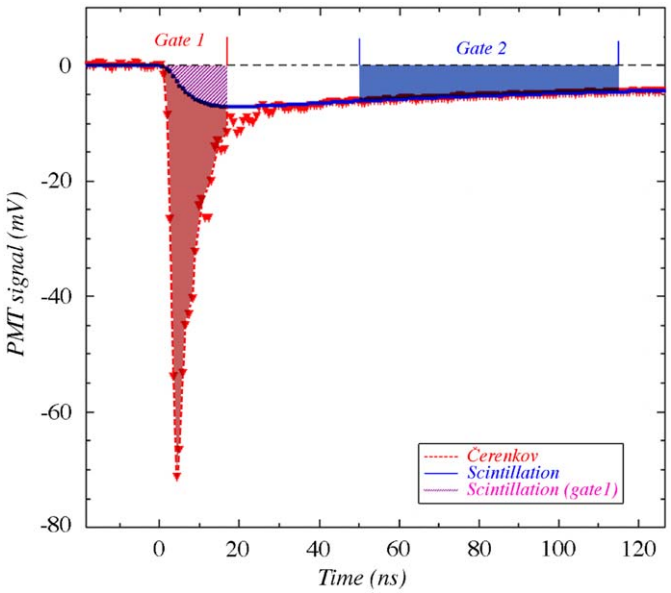

Fig. 5. The time structure of a typical shower signal measured in the BGO em calorimeter equipped with a UV filter. These signals were measured with a sampling oscilloscope, which took a sample every 0.8 ns. The UV BGO signals were used to measure the relative contributions of scintillation light (gate 2) and Cherenkov light (gate 1).

We have applied the same techniques in the present series of measurement. The four PMTs that detected the light produced in the BGO crystal matrix were equipped with UV filters.[11] These filters were transparent for light in the wavelength region from 250 to 400 nm, which harbors a large fraction of the Cherenkov light, plus a small fraction of the scintillation light, which peaks around 480 nm. The time structure of the signals from the PMTs clearly exhibited these two components, as illustrated in Fig. 5. The (prompt) Cherenkov component is represented by the sharp peak, whereas the long tail has the same characteristic time structure as pure scintillation signals generated in this crystal, i.e., an exponential decay with a time constant of 300 ns.

The signals from the PMTs that detected the light transmitted through the UV filters thus contained event-by-event information about the relative contributions of both Cherenkov and scintillation photons. We have used the oscilloscope data to extract this information, as follows. For every event, the integrated charge collected in the time interval from 50 to 115 ns after the start of the pulse was used as a measure for the scintillation signal produced in that event, while the charge collected from 0 to 16 ns was used as the basis for the measurement of the Cherenkov signal. However, there was always some scintillation light that contaminated the latter signal. From detailed studies of the time structure of the unfiltered (i.e., almost pure scintillation) signals, we concluded that the integrated charge due to scintillation light collected in the time interval from 0 to 16 ns after the start of the pulse amounted to 20% of the charge collected from 50 to 115 ns.

[11] UG11glass transmission filter (Schott). See Ref. [7] for details on the properties of this filter.

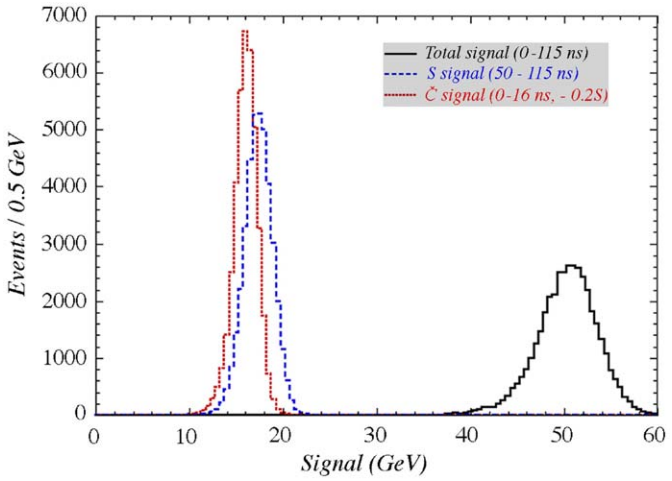

Fig. 6. Signal distributions for 50 GeV electrons in the BGO em calorimeter equipped with a UV filter. These signals were measured with a sampling oscilloscope, which took a sample every 0.8 ns. The signal distributions concern the total charge collected during 115 ns after the start of the pulses, and the charge collected during gate 2 (scintillation light) and gate 1. The latter signal was corrected for the contribution of scintillation light, so that the pure Cherenkov contribution to this "prompt" component remained.

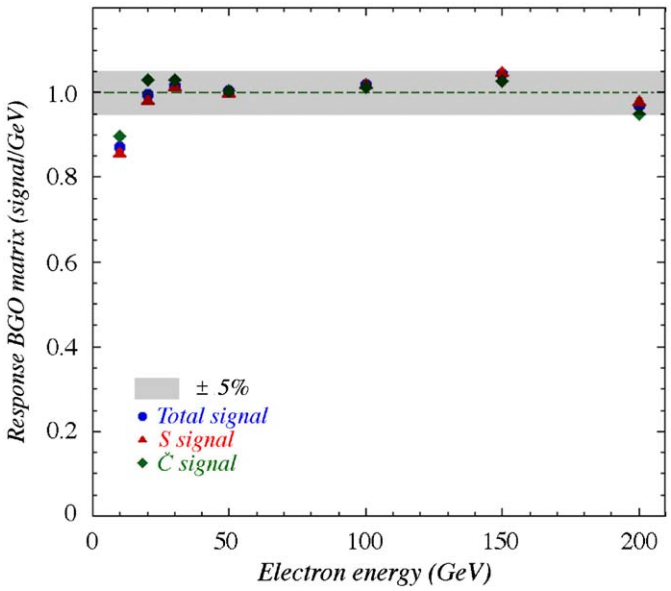

Fig. 7. The response of the BGO ECAL as a function of energy, for electrons with energies ranging from 10 to 200 GeV. The average signal per unit of energy is plotted versus the beam energy, separately for the scintillation and Cherenkov components of the signals, and for the total signal, integrated over the first 115 ns. See text for details.

On this basis, it was possible to determine this contamination of the "prompt" signal event by event as well.

We have used this procedure to complete the calibration of the BGO signals, described in Section 2.4 (which provided the *intercalibration* constants a_k for the signals from the four PMTs). Fig. 6 shows the total signal distribution for 50 GeV electrons, integrated over 115 ns, as well as the scintillation and Cherenkov signal distributions, obtained as described above. The latter two distributions were centered around 18 and 16 GeV, respectively. These two distributions were boosted separately to 50 GeV by means of overall calibration constants C_S (50/18) and C_C (50/16). The (six) calibration constants (a_k, C_S and C_C) have been used throughout the analyses described in this paper.

4. Experimental results

4.1. Electron detection

Electron beams of different energies were used to study the characteristics of the performance of the BGO ECAL in this unusual geometry. In particular, we studied the *signal linearity*, the *response uniformity* and the *energy resolution*. For the linearity and the resolution measurements, the beam was steered into the central region of the detector, i.e., along trajectory *c* (see Fig. 4).

The results of the signal linearity measurements are shown in Fig. 7, where the calorimeter *response*, i.e., the average signal per unit energy, is plotted as a function of the beam energy, separately for the total signal, integrated over the first 115 ns, as well as for the scintillator and Cherenkov signals, as defined above. Over the energy range of 20–200 GeV, the BGO em calorimeter turned out to be linear to within $\approx \pm 5\%$, the area marked gray in Fig. 7. The response at 10 GeV was 10–15% smaller than the average value for the other energies. We ascribe this to the fact that the PMTs were more or less blind to energy deposited in the first row of crystals encountered by the incoming beam particles. The same was true for energy deposited in the last row. This phenomenon mostly affected the showers with the lowest and the highest energies, respectively. The importance of the energy dependence of the longitudinal shower shape (and thus the importance of these

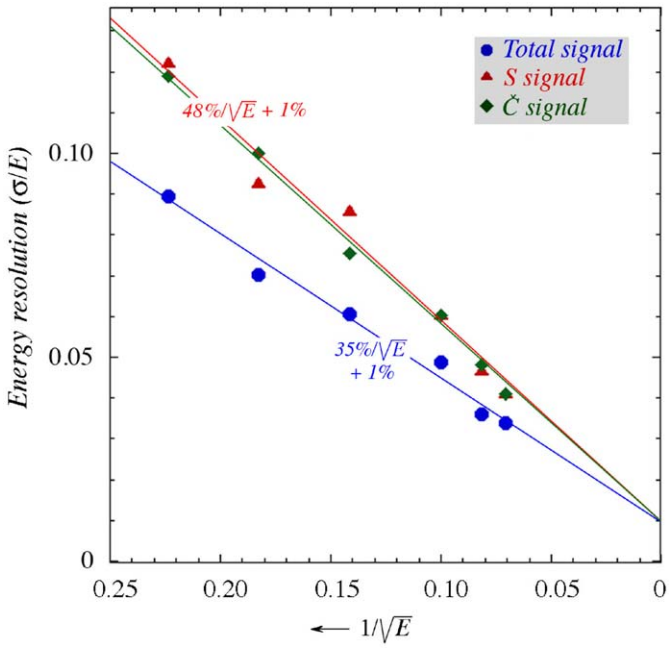

Fig. 8. The energy resolution of the BGO ECAL as a function of energy, for electrons with energies ranging from 20 to 200 GeV. The relative width of the distribution, σ/mean, is plotted versus the beam energy, separately for the scintillation and Cherenkov components of the signals, and for the total signal, integrated over the first 115 ns. See text for details.

inefficient crystal rows) may be illustrated by the fact that the measured ratio of the signals observed in PMTs 1,2 and PMTs 3,4 changed from 4.1 at 10 GeV to 2.0 at 50 GeV and 1.8 at 200 GeV. These numbers were reproduced by Monte Carlo simulations of em shower development in the crystal matrix. These simulations also supported the above explanation for the observed non-linearity.

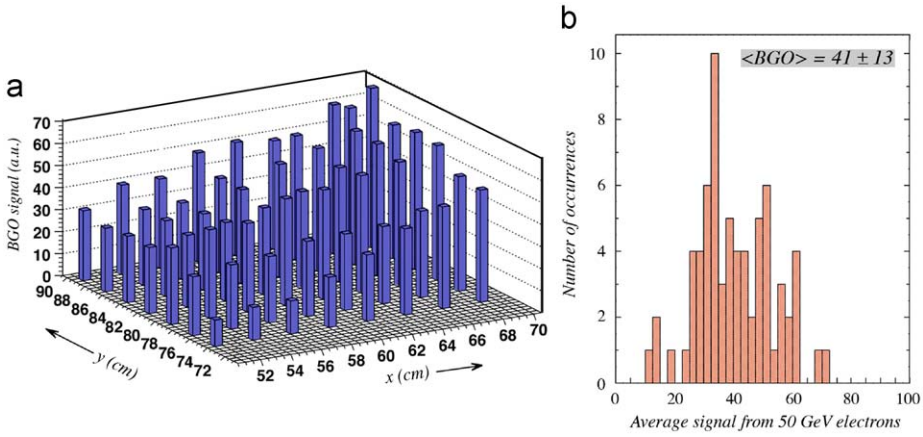

Fig. 9. The response uniformity of the BGO ECAL for 50 GeV electrons. The average scintillator signal, integrated over a time interval from 50 to 115 ns after the start of the pulse (gate 2, see Fig. 5), is shown as a function of the impact point of the beam particles (a). The averages obtained for the various impact points covering the front face of the crystal matrix are shown in diagram (b).

At each electron energy, the energy resolution was determined from a Gaussian fit to the signal distribution. As indicated by Fig. 6, such fits gave a reasonable description of the signal distributions. The ratio of the width (σ) and the mean value of the signal distributions is plotted as a function of energy in Fig. 8, both for the total signal (integrated over the first 115 ns), as well as for the scintillation and Cherenkov signals. The energy is plotted on a scale linear in $E^{-1/2}$, running from right to left, so that scaling of the energy resolution with $1/\sqrt{E}$ is represented by a straight line through the bottom right corner in this plot. The various straight lines are the result of fits of the experimental data to an expression of the type

$$\sigma/E = \frac{a_1}{\sqrt{E}} + a_0. \quad (1)$$

It turns out that such an expression describes the experimental data quite well for a scaling term of $a_1 = 0.35$ in case of the total BGO signals and $a_1 = 0.48$ both for the scintillation and the Cherenkov signal components. The deviation from $E^{-1/2}$ scaling is well described by a constant term $a_0 = 0.01$ in all cases.

One factor that contributed to the width of the signal distributions at all energies, and thus to a deviation from $E^{-1/2}$ scaling, is *signal non-uniformity*, i.e., a position dependent calorimeter response. For the uniformity measurements, the 50 GeV electron beam was moved in steps of 2.5 cm over a grid spanning an area of $20 \times 20\,\mathrm{cm}^2$, for a total of 81 different impact points.

The results of these uniformity measurements are displayed in Fig. 9. In Fig. 9a, the average values of the scintillation signal distributions are shown in the form of a legoplot, covering the central area of the BGO crystal matrix. In Fig. 9b, the same data are plotted in a histogram. These results clearly illustrate the inadequacies of the readout scheme of the BGO matrix (see Section 2.1). The response clearly depended both on the thickness of the crystals and on the distance from the exit face at which the light was produced (see Fig. 1 for the coordinate axes).

The width (σ_{rms}) of the histogram in Fig. 9b represents 32% of the average signal: 12.9 GeV for an average reconstructed energy of 40.5 GeV. The results obtained for the Cherenkov component were very similar.

Another contribution to the energy resolution came from fluctuations in "undetected energy", deposited in crystals to which the PMTs were blind. The Monte Carlo simulations mentioned above indicated that at 10 GeV, such fluctuations contributed more than 6% to the measured resolution, and at 200 GeV almost 2%.

4.2. The quality of the BGO dual-readout calorimeter

If photoelectron statistics were the only factor contributing to the energy dependent term in the energy resolution, the results shown in the previous section (Fig. 8) would mean that the total signals produced in the PMTs detecting the light produced in the BGO ECAL and transmitted through the UV filters were constituted by only 10 photoelectrons for each GeV deposited energy. The scintillation and the Cherenkov signals would each consist of only 4 photoelectrons per GeV. This is even less than the light yield of the Cherenkov fibers in the hadronic (fiber) section of the calorimeter system, for which we measured 8 photoelectrons per GeV [6].

This small light yield was a consequence of the extremely poor (or rather the absence of) optical coupling between the BGO crystals and the PMTs, together with the fact that we detected Cherenkov light produced at the unfavorable angle of 90° with the direction of the showering particles.[12] Owing to the large index of refraction of the BGO crystals, most of the light hit the crystal/air interface at such an angle that it did not leave the crystal at all, at least not at the small end face, because of total internal reflection.

Each PMT had a photocathode surface of $\sim 40\,\mathrm{cm}^2$, i.e., equivalent to the surface of seven BGO crystals. The total photocathode surface of the four PMTs thus corresponded to only one quarter of the exit surface of the BGO matrix. Probably, the quantum efficiency also varied over the photocathode surface. Also, and especially, the combined effects of light attenuation and light trapping through internal reflection in the tapered crystals made the response strongly dependent on the distance the light had to travel from the (x) position where it was generated to the light detector [7]. These effects, in combination, were responsible for the large non-uniformity observed in Fig. 9, and for the deviation from $E^{-1/2}$ scaling observed when the electron beam hit the matrix in the same spot (Fig. 8).

The BGO matrix that served as the electromagnetic calorimeter section in these measurements was, in terms of the crucial properties of light yield and response uniformity, worse than the hadronic (fiber) calorimeter section. Therefore, one should not expect an improvement in the quality of hadronic shower detection in this calorimeter system, compared to that of the fiber calorimeter in stand-alone mode [4]. In order to achieve such

[12] At this angle, the measured Cherenkov light intensity was measured to be about half of that at the Cherenkov angle of 63° [7].

an improvement, the readout of the BGO matrix would have to be changed such as to improve its crucial properties, for example by equipping each individual crystal with a photon detector in good optical contact. This modification would then also lead to the electron resolution one has come to expect from crystals. Such a solution was beyond the scope of these tests (see Section 2.1).

4.3. Hadron detection

Results on the stand-alone performance of the DREAM fiber calorimeter were reported in a previous paper [4]. In the present study, we have focused primarily on the effects of the BGO electromagnetic section and the leakage counters.

By selecting events in which the pions started a shower *beyond* the BGO ECAL, we could test the fiber calorimeter in stand-alone mode. As we saw earlier, the energy resolution was in that case limited by fluctuations in side leakage. For example, at 100 GeV, this side leakage amounted to 9.7%, on average, in the scintillator channel. Because of the different shower profiles, the lateral leakage was about 40% smaller in the Cherenkov channel [10].

The leakage counters installed during the present measurements made it possible to verify the effects of lateral shower leakage on the calorimeter performance. The scintillator paddles that constituted the leakage counters only provided information about the leakage in the scintillator channel, since Cherenkov light was a negligible fraction of the total leakage signal and in any case undistinguishable. For this reason, the leakage signals were only added to the scintillation signals produced by the calorimeter system.

As described in Section 2.4, the leakage counters were calibrated in units of *mips*. Based on the observed signals and on the lateral shower profiles mentioned above, the leakage signals could be converted from *mips* into energy units: 1 *mip* was found to be equivalent to 0.37 GeV energy deposit.

It turned out that the average signal in these leakage counters was clearly anti-correlated to the em shower fraction, f_{em}. For pions that started their shower in the fiber calorimeter, f_{em} could be derived from the Cherenkov/scintillator signal ratio (C/S) in a straightforward way, since

$$\frac{C}{S}=\frac{f_{em}+0.21(1-f_{em})}{f_{em}+0.77(1-f_{em})} \quad (2)$$

where 0.21 and 0.77 represent the h/e ratios for the quartz and scintillator readout structure, respectively [4].

Fig. 10 shows the measured relationship between the average leakage signal and the (uncorrected) f_{em} value. There is a very clear anti-correlation: The larger f_{em}, the smaller the average leakage signal. This is completely consistent with the expectation that showers with a large em component are better contained, because of the fact that the em shower component is more strongly concentrated around the shower axis. The f_{em} dependence of the leakage signals is well described by an exponential relationship, for all three pion energies considered here (50, 100 and 300 GeV). The average leakage signal decreased by about a factor of two over the full f_{em} range. For a given f_{em} value, the leakage signal was, on average, also approximately proportional to the energy of the showering hadron.

Since the leakage signals seemed to provide, on average, a reasonable measurement of the energy leaking sideways out of the calorimeter, we also studied the extent to which the hadronic energy resolution was improved by taking the leakage signals into account.

Fig. 11 shows the effects of adding the leakage signals. The energy resolution for single pions with and without the contribution of the leakage signals to the scintillator signals is plotted as a function of the pion energy. Since the response function exhibited the usual deviations from a Gaussian line

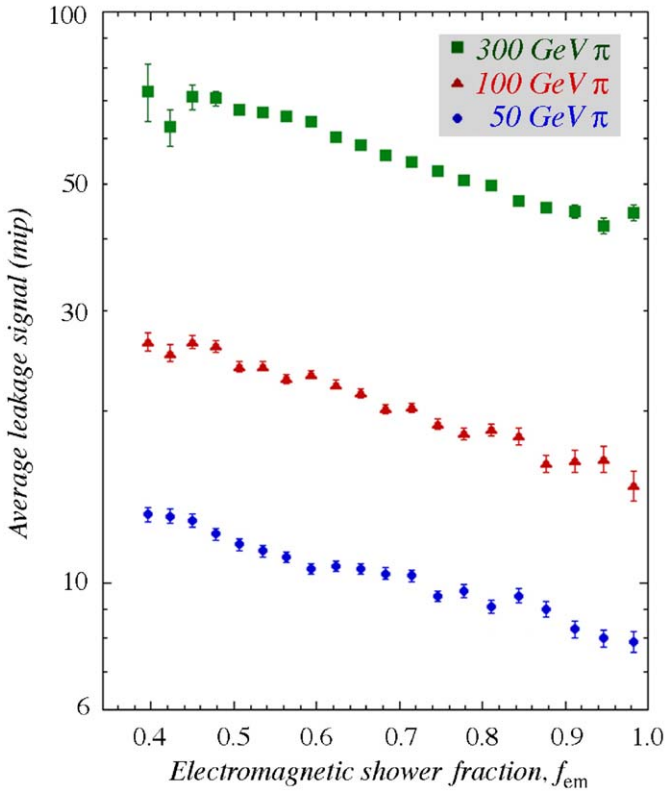

Fig. 10. Average leakage signal, as a function of the em shower fraction measured in the DREAM fiber calorimeter, for pions of three different energies that penetrated the BGO ECAL without starting a shower. The leakage signal is expressed in *mips*, 1 *mip* is equivalent to an energy deposit of 0.37 GeV.

shape (see, e.g., Fig. 14), the energy resolution was calculated as σ_{rms}/E for this purpose. The events were subdivided into two samples: events where the pions penetrated the BGO ECAL without starting a shower ("mip-in-BGO", Fig. 11a), and events where the shower started in the crystal matrix ("non-mip-in-BGO", Fig. 11b). The runs with the lowest (20 GeV) and the highest (300 GeV) energy were left out of the mip-in-BGO sample. The large contamination by unidentified muons (low energy) or the effects of longitudinal shower leakage (high energy) caused the event samples to be biased in these cases.

Both in Fig. 11a and b, we see that adding the leakage signals led to an improvement of the energy resolution, typically $\sim 10\%$ in the mip-in-BGO sample, and $\sim 15\%$ for the events in which the pion shower started in the crystal matrix. The somewhat smaller improvement in the first sample may be due to the fact that this sample contained events in which the showers started deep inside the calorimeter system. In such events, most of the leakage occurred longitudinally, into an area not covered by leakage detectors.

4.4. Multiparticle detection

One of the main purposes of the tests described in this paper was to see if and to what extent the dual-readout principles, which worked so well to improve the hadronic performance of the stand-alone fiber calorimeter [4], are also applicable when most of the shower energy is deposited in a crystal calorimeter section. For reasons spelled out in Section 2.2, a very good way to study this is with high-multiplicity multi-particle events, created by pions impinging on a target installed upstream of the calorimeter

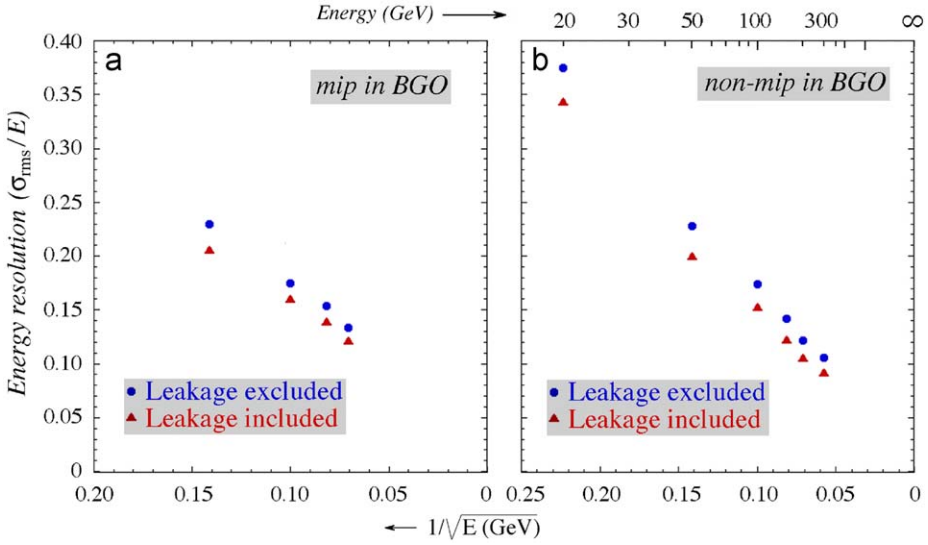

Fig. 11. Energy resolution for single pions that penetrated the BGO ECAL without starting a shower, measured with the scintillation signals alone. Results are given with and without taking into account the signals from the leakage counters (a). Energy resolution for single pions that started their shower in the BGO ECAL, measured with the scintillation signals alone. Also here, results are given with and without taking into account the signals from the leakage counters (b).

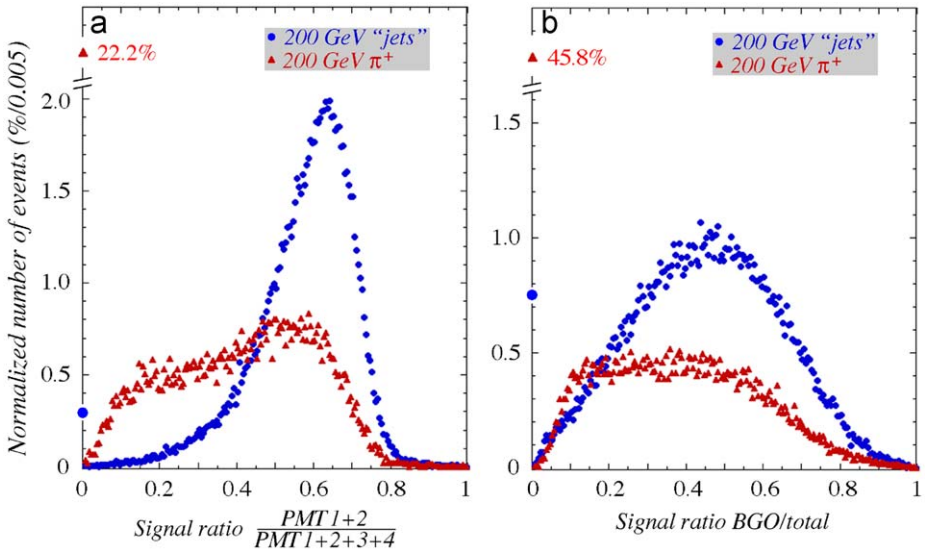

Fig. 12. Comparison of some characteristics of the BGO crystal matrix for 200 GeV beam pions and 200 GeV multi-particle "jets". Shown are the fraction of the total BGO signal detected in PMTs 1/2 (a) and the fraction of the total scintillator signal detected in the BGO crystal matrix (b). The event sample used for the left diagram consisted only of the events that started to shower in the BGO crystal matrix, for the right diagram all events were used. All distributions have been normalized to the same surface area.

system. In such events, a collection of secondaries, primarily photons (from π^0 decay) and pions, hit the calorimeter simultaneously, at different impact points. The photons deposited all their energy in the BGO matrix, while the pions started hadronic showers at various depths inside the combined calorimeter system. These multi-particle events were more relevant for our stated purpose than the events induced by single beam pions, because:

(1) the showers developed over the entire volume of the BGO crystal matrix, not just the region near the beam axis, and
(2) the fraction of the shower energy deposited in the crystal calorimeter section was, on average, considerably larger than for single-particle events.

In fact, these two effects could also be "tuned" through the threshold value of the signal recorded in the ITC scintillation counter placed directly downstream of the interaction target (see Fig. 3). Some results illustrating these effects for the "standard" threshold of 10 *mips* are shown in Fig. 12, where 200 GeV "jets" are compared with 200 GeV single pions.

Fig. 12a shows the fraction of the total BGO signal recorded in the PMTs located upstream (PMTs 1,2, see Fig. 3). Only events where more than 5 GeV was deposited in the crystal matrix were considered in this case. On average, 58% of the "jet" signal was recorded in these upstream PMTs, versus only 33% for single pions. In fact, in 22.2% of the pion events no signal at all was recorded in these two PMTs, since the pion started its shower deeper inside the crystal matrix. Because of the photons that typically constituted a significant fraction of the "jet" energy, and

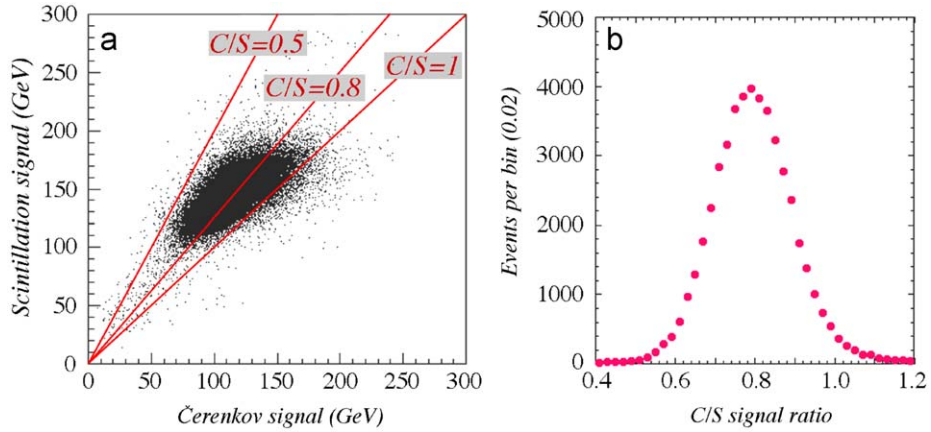

Fig. 13. Scatter plot of the Cherenkov versus the scintillator signals for the 200 GeV "jet" events. Every event is represented by a dot (a). Distribution of the C/S signal ratio measured for this event sample (b). The signals from the leakage counters were taken into account in determining the scintillation signal.

which developed showers directly upon entering the crystal, there was no equivalent for this effect in the case of the "jets". Only in a very small fraction of the events (0.3%), the "jet" exhibited the characteristics of a penetrating single pion. These are presumably events from the Landau tail, in which a single pion did in fact *not* interact in the upstream target, but lost an anomalous amount of energy traversing the ITC counter, and thus passed the threshold applied for "jets".

Fig. 12b shows the fraction of the total shower energy that was deposited in the BGO crystal matrix. Also in this case, there were large differences between "jets" and single pions. The most striking difference concerned the fact that almost half of the single pions (45.8%) traversed the ECAL without starting a shower. Only 0.7% of all "jet" events exhibited this characteristic. As before, these are most likely events from the Landau tail in the ITC counter. On average, 45% of the total energy was deposited in the BGO crystal matrix for the "jet" events, versus only 21% for the single pions. These characteristics indicate that the "jet" event samples were indeed better suited to test the hadronic performance of the crystal matrix than the single pions.

All distributions shown in Fig. 12 were normalized, and therefore the surface areas under the different distributions are equal. As expected, the observed differences between the "jet" and single-pion event samples were further enhanced when the threshold on the ITC signal was increased.

The crucial aspect of the DREAM procedure is the comparison of the scintillation and Cherenkov signals produced in hadronic shower development. The ratio between these two signals is a measure for the em shower fraction. In the case of the fiber detector in stand-alone mode, there is a simple one-to-one correspondence between this signal ratio and f_{em}, given by Eq. (2). For the combined BGO+fiber system, such a simple relationship does not exist, since the e/h values of the BGO crystal are different from those of the fiber detector, and the energy sharing between these two calorimeter systems varied from event to event. However, also in this case, the ratio of the Cherenkov and scintillator signals itself (to be called the C/S ratio in the following) should be a good measure for the em shower content.

The distribution of the C/S signal ratio measured for our standard sample of 200 GeV "jet" events is shown in Fig. 13b. The contributions of the signals from the leakage counters to S were taken into account when calculating this signal ratio. The figure shows a broad distribution extending from $C/S \sim 0.4$ to 1.2. Fig. 13a shows a scatter plot of the Cherenkov versus the scintillator signals for the same event sample. Every event is represented by a dot in this diagram. The projection of the

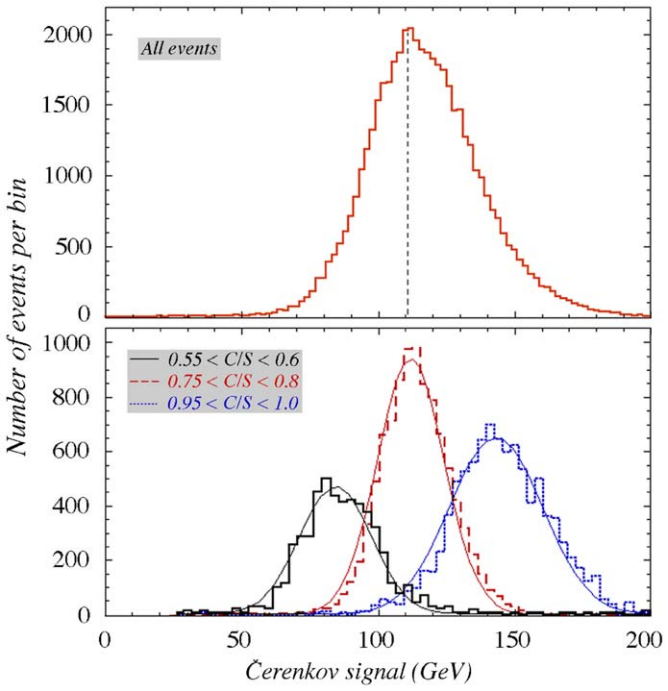

Fig. 14. The Cherenkov signal distribution for 200 GeV "jet" events detected in the BGO+fiber calorimeter system (a) together with the distributions for subsets of events selected on the basis of the ratio of the total Cherenkov and scintillation signals in this detector combination (b).

distribution of these dots on the horizontal axis represents the total Cherenkov signal distribution, the projection on the vertical axis the scintillator signal distribution. Events with the same C/S value are located on straight lines through the bottom left corner, such as the $C/S = 0.5$, 0.8 and 1.0 lines drawn in this plot.

The fact that the dots in Fig. 13a are *not* clustered around a fixed C/S value means that the two signals provided complementary information, which may be used to improve the performance offered by either one of them.

This is illustrated in Fig. 14. Fig. 14a shows the projection of the scatter plot on the horizontal axis, i.e., the distribution of the total Cherenkov signal. This signal is broad, asymmetric (non-Gaussian) and centered around a value of only 110 GeV, whereas the total "jet" energy was 200 GeV. Fig. 14b shows three different subsets of events, selected on the basis of the measured C/S signal ratio.

These three distributions are narrower, well described by Gaussian fits and centered at a value that increases roughly proportionally with the C/S value of the selected event sample. This is precisely what was observed for the fiber calorimeter in stand-alone mode, and what allowed us to eliminate the effects of fluctuations in f_{em} in that calorimeter [4].

The overall signal distribution (Fig. 14a) is simply a superposition of many (Gaussian) distributions such as the ones shown in Fig. 14b, and the asymmetric shape just represents the extent to which "jets" with different em fractions occurred in the entire event sample.

The results for the scintillation signals, obtained by projecting the scatter plot on the vertical axis, were less spectacular, because of the fact that the e/h ratios for this signal component deviated less from 1.0 than in the Cherenkov case. Yet, they confirmed in essence the trends shown in Fig. 14. In particular, the signal distributions for the three subsets of events selected on the basis of the C/S signal ratio were much better described by Gaussian fits than the overall scintillator signal distribution. The mean values of these distributions increased from 145 to 148 GeV as the C/S signal ratio increased. The fact that the performance improvements that could be made on the basis of the measured Cherenkov/scintillation signal ratios is much smaller for the scintillation component of the calorimeter signals than for the Cherenkov component is commensurate with results obtained for the stand-alone fiber calorimeter module [4].

4.5. DREAM procedures for a hybrid calorimeter system

The DREAM corrections, described in detail in Ref. [4] for the stand-alone fiber calorimeter, constitute a simple procedure in which the measured signal for each individual event is increased such as to make the C/S ratio for that event equal to 1.0, i.e., the value for em showers. The validity of this correction is based on the linear relationship that should be and was measured to exist between the measured signals and the f_{em} value. As mentioned above, in the case of this hybrid calorimeter system, there is no straightforward way to determine the f_{em} value of the events, because of the fact that the ECAL crystal matrix and the fiber HCAL have different e/h values. We have nevertheless applied the correction procedure described in Ref. [4], using the relationship between C/S and f_{em} (Eq. (2)) for the entire calorimeter, and not just for the fiber component for which it is exactly valid.

The relationship between the measured total Cherenkov signal and the f_{em} value derived on this basis is shown in Fig. 15a. The figure also shows a dashed line depicting the relationship one should expect if the entire calorimeter had indeed an h/e value of 0.21 ($e/h = 4.7$) for Cherenkov signals and $h/e = 0.77$ ($e/h = 1.3$) for scintillation signals:

$$C_{tot} = E[0.21 + 0.79 f_{em}]. \quad (3)$$

The relationship between the total Cherenkov signals and the f_{em} values measured for 200 GeV "jets" with the fiber calorimeter in stand-alone mode is represented by the dotted line in Fig. 15a. Energy absorbed in the upstream target and carried by reaction products that physically missed the calorimeter were considered responsible for the 5% difference between the dashed and dotted curves [4].

A comparison between the f_{em} values derived from the C/S signal ratios in the hybrid calorimeter system and the dashed and dotted curves shows much larger differences. At $f_{em} = 1$, the pivotal point for the dual-readout correction, the total Cherenkov signal was 25% smaller than the beam energy and 20% smaller than the value measured with the stand-alone fiber module.

Nevertheless, also in this hybrid calorimeter system, the measured total Cherenkov signals did exhibit a linear relationship with the f_{em} values determined in this way. This is indicated by the solid line in Fig. 15a. The intercept for $f_{em} = 0$ found from a linear fit to the experimental data in the range $0 < f_{em} < 1$, which is determined by the effective h/e ratio, was approximately the same as for the stand-alone data and Eq. (3).

If we used the f_{em} values found with the described procedure to correct the measured total Cherenkov signals, then the measured signal distribution, shown in Fig. 15b, was transformed into the one shown in Fig. 15c. This distribution shows indeed several of the characteristics that we observed earlier as a result of the same procedure applied to the fiber calorimeter in stand-alone mode [4]: the signal distribution became narrower, much more symmetric and its central value shifted towards the beam energy. Yet, the results were considerably less spectacular for our hybrid calorimeter system. In particular, the improvement in

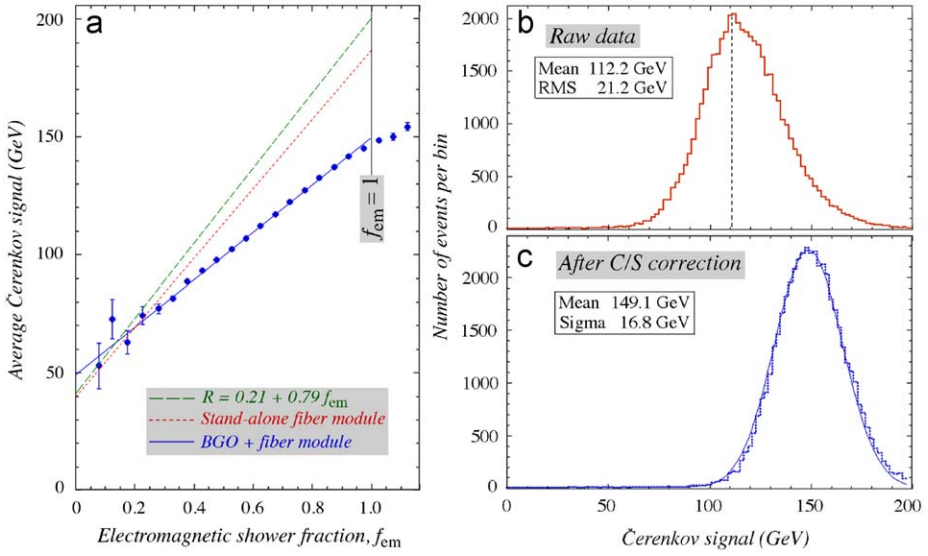

Fig. 15. The average Cherenkov signal for 200 GeV multi-particle events ("jets") as a function of the em shower fraction, f_{em}, determined on the basis of Eq. (2) from the total Cherenkov/scintillator signal ratio. The dashed line represents Eq. (3) and the dotted line the relationship measured for 200 GeV "jet" events for the fiber calorimeter in stand-alone mode [4] (a). Cherenkov signal distributions for 200 GeV multi-particle events before (b) and after (c) applying the dual-readout corrections derived event by event from these f_{em} values.

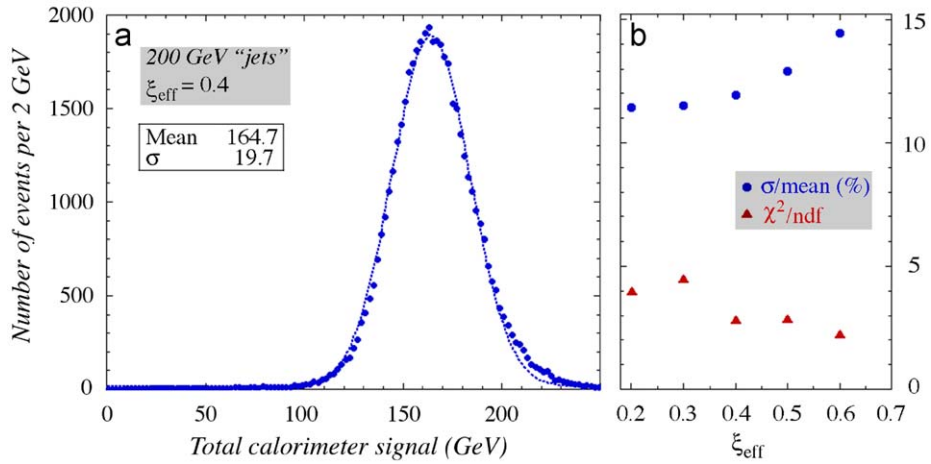

Fig. 16. The total signal distribution for 200 GeV "jet" events detected in the BGO+fiber calorimeter system, corrected for the effects of fluctuations in f_{em} by means of Eq. (4) (using $\xi_{eff} = 0.4$), together with the result of a Gaussian fit to these data (a). The dependence of the energy resolution and the χ^2 of the Gaussian fit to the value of the parameter ξ_{eff} (b).

energy resolution was not as impressive, and the shift in reconstructed energy was by no means sufficient to approach the beam energy.[13]

We have also tried another method to implement the DREAM corrections, which did *not* rely upon an event-by-event determination of f_{em}. Eq. (3) and its equivalent for the scintillation signals represent two equations with two unknown quantities, the em energy fraction f_{em} and the energy E. Solving these equations for E leads to

$$E = \frac{S - \xi C}{1 - \xi} \quad \text{with } \xi = \frac{1 - (h/e)_S}{1 - (h/e)_C}. \tag{4}$$

For the fiber module, the value of ξ amounts to $0.23/0.79 \sim 0.3$. On the other hand, we estimated that BGO has an $(e/h)_S$ of ~ 2.0, so that ξ would be ~ 0.6 for the crystal matrix. For showers developing partly in the BGO matrix and partly in the fiber module, we would thus have to use an "effective" ξ value somewhere in between 0.3 and 0.6. We have applied Eq. (4) for various values of ξ_{eff} in the range from 0.2 to 0.6. The resulting energy resolution and the χ^2 of a Gaussian fit to the corrected signal distribution are shown in Fig. 16b, as a function of ξ_{eff}, for 200 GeV "jets". Fig. 16a shows the signal distribution for 200 GeV "jets" using $\xi_{eff} = 0.4$, together with the result of a Gaussian fit, which described the experimental data somewhat better than with the previous method. The reduced χ^2 of this Gaussian fit (χ^2/ndf) amounted to 112/40, versus 172/40 for the fit to the distribution in Fig. 15c, which was obtained on the basis of an event-by-event estimate of f_{em}. Also the reconstructed energy was considerably better with this alternative method: 165 GeV, versus 150 GeV for Fig. 15c. The resolutions were about the same in both cases.

We have tried the same method, with the same ξ_{eff} values, for the other "jet" energies, and found that the results were better for these energies as well. Especially at the lowest energies (50 GeV), there was a very clear dip in the χ^2 of the Gaussian fit near $\xi_{eff} = 0.45$. Compared to this dip, the χ^2 value doubled when ξ_{eff} was increased to 0.6 and tripled for $\xi_{eff} = 0.3$ (Fig. 17).

We therefore conclude that the method represented by Eq. (4) is apparently preferable for eliminating the effects of fluctuations in f_{em} on the signals from this hybrid calorimeter system. In addition, it is more transparent and simpler to apply, since it only involves one constant factor (ξ_{eff}) in addition to the two measured signals.

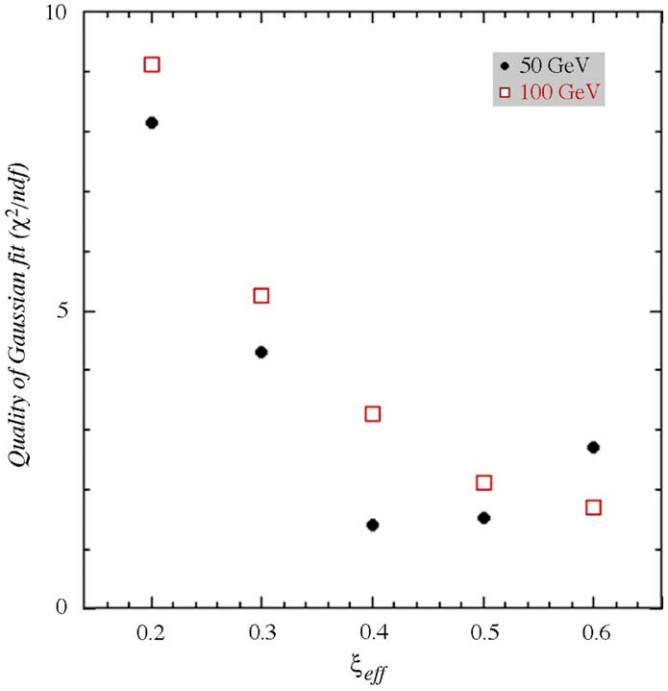

Fig. 17. The χ^2 of a Gaussian fit to the signal distribution of 50 and 100 GeV "jets" corrected for the effects of fluctuations in the em shower fraction by means of Eq. (4), as a function of the value of the parameter ξ_{eff}.

Results on the response and the energy resolution as a function of energy are shown in Fig. 18. The figure also shows the results obtained for "jets" of the same energies measured in the fiber calorimeter alone [4]. One may wonder why the effects of the DREAM corrections on the measured signal distributions were so different for this hybrid calorimeter system, compared to the stand-alone fiber calorimeter. Even though the corrections made the signal distributions approximately Gaussian, the energy resolution could be much better, and the value of the

[13] In these multi-particle events, some losses due to energy absorbed in the production target and secondaries produced at such large angles that they missed the calorimeter are inevitable. However, these losses should not exceed more than 10% of the nominal beam energy [4].

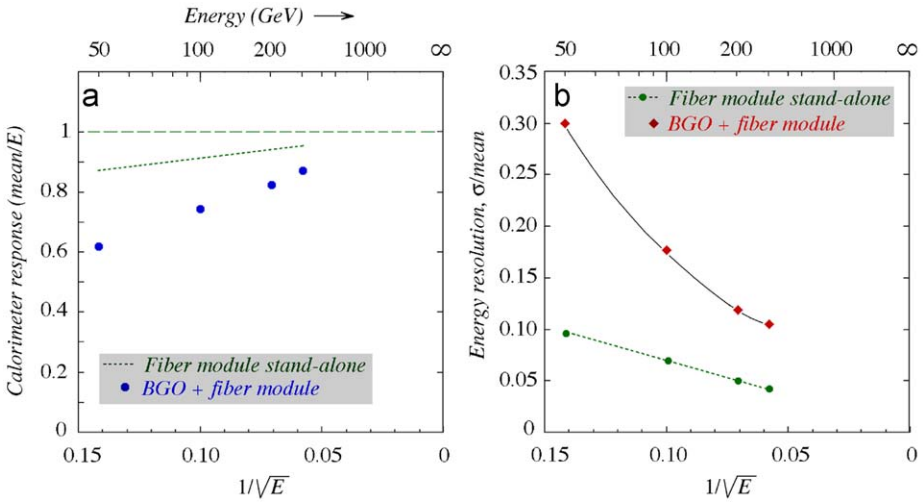

Fig. 18. The calorimeter response (a) and the energy resolution (b) for "jet" events detected in the BGO + fiber calorimeter system, corrected for the effects of fluctuations in f_{em} by means of Eq. (4) (using $\xi_{eff} = 0.4$), as function of the "jet" energy. The results obtained previously for the fiber calorimeter module in stand-alone mode [4] are indicated by dotted lines.

reconstructed energy was too low. Moreover, the energy resolution did not scale with $E^{-1/2}$, while this was an important characteristic of all methods that were used to eliminate the effects of f_{em} fluctuations in the DREAM fiber calorimeter [4,13]. Based on the energy dependence of the observed effects (Fig. 18), we believe that the following effects are responsible for these differences:

- The non-uniformity of the signals from the BGO crystal matrix. Contrary to the electron beams with which this matrix was calibrated and which entered the detector always at the same spot, the multi-particle events used in this study illuminated *the entire matrix*. Therefore, the response differences observed in the grid scan (Fig. 9) affected the "jet" signal distributions in a major way. Fig. 9b shows an rms spread of 32% about the average response value. If we assume that a typical multi-particle event consisted of 10 different particles developing showers in the ECAL, then one should expect an energy-independent contribution to the energy resolution of $32\%/\sqrt{10} \approx 10\%$ from this effect alone. This effect would cause a deviation from $E^{-1/2}$ scaling.
- The same grid scan also shows that the average response of the crystal matrix was considerably smaller than the response obtained in the points at which the detector was calibrated (41 GeV for 50 GeV electrons), Of course, this difference causes the reconstructed energy to be too low, more so at lower energies. Therefore, the non-uniformity both affected the energy resolution and the reconstructed "jet" energy.
- The PMTs reading the signals from the crystal matrix only covered the central portion of that matrix efficiently. In particular, the PMTs were more or less blind to light produced in the first row of crystals encountered by the showering particles. This effect explained the non-linearity observed at the lowest energies (10–15% at 10 GeV, see Fig. 7). Since the multi-particle threshold on the ITC signals was 10 mips, and since the number of photons (from π^0 decay) in these multi-particle events was, on average, equal to the number of charged reaction products, we conclude that the "jets" selected for our study contained typically at least 10 γs developing showers in the crystal matrix, with typical energies of less than 10 GeV in the 200 GeV sample. Therefore, the response of the crystal matrix to this photon component was even lower than suggested by the non-uniformity effects discussed above. This effect led to a further reduction of the reconstructed "jet" energy. And again, it was relatively larger at lower "jet" energies.
- Finally, the light yield of the crystal matrix was so low that it affected the width of the distributions. A Cherenkov light yield of 4 photoelectrons per GeV deposited energy translates for 100 GeV em energy into an energy resolution of 5%. Especially at the lower jet energies, this effect might have contributed to a noticeable broadening of the multi-particle signal distributions.

All these effects could of course have been avoided if the crystal matrix had been custom-made for this application.

5. Conclusions

We have demonstrated that the dual-readout principles, which allow for an important improvement of the performance of hadron calorimeters, can also be applied in a hybrid calorimeter system consisting of a BGO crystal matrix, followed by a fiber-based dual-readout calorimeter. High-multiplicity multi-particle events which deposited, on average, about half of their total energy in the crystal matrix were used for this study. It turned out that the time structure of the BGO signals made it possible to classify these events in terms of their em shower content in the same way as for the stand-alone fiber calorimeter, where the em fraction can be directly measured from the ratio of the Cherenkov and scintillator signals. This information could subsequently be used to improve the hadronic energy resolution and signal linearity, and led to a Gaussian response function.

These results were obtained despite the fact that crucial properties of the crystal matrix used in these studies were far from ideal. In particular, the light yield was only a small fraction of what it could have been with a state-of-the-art readout system, and the response uniformity left very much to be desired. These characteristics limited the improvement of the energy resolution and impeded a completely correct reconstruction of the energy of the showering hadrons, which is one of the hallmark virtues of the dual-readout method.

Studies with single pions, in which typically only a small fraction of the beam energy was deposited in the crystal matrix, indicated that a dominating factor limiting further improvement of the energy resolution was side leakage. We have demonstrated

that a very primitive leakage detector already made a noticeable improvement in this respect.

Because of the mentioned inadequacies of the experimental setup, considerably better results may be expected for a sufficiently large calorimeter of this type (radius ≥ 30 cm), equipped with an optimized readout system. We are planning to build and test such a detector.

Acknowledgments

We thank CERN for making particle beams of excellent quality available. This study was carried out with financial support of the United States Department of Energy, under Contract DE-FG02-07ER41495.

References

[1] R. Wigmans, New J. Phys. 10 (2008) 025003.
[2] P. Mockett, in: Proceedings of the 11th SLAC Summer Institute on Particle Physics, July 1983 ⟨www.slac.stanford.edu/pubs/confproc/ssi83-008.html⟩.
[3] D.R. Winn, W.A. Worstell, IEEE Trans. Nucl. Sci. NS-36 (1) (1989) 334.
[4] N. Akchurin, et al., Nucl. Instr. and Meth. A 537 (2005) 537.
[5] R. Wigmans, Quartz fibers and the prospects for hadron calorimetry at the 1% resolution level, in: Proceedings of the VIIth International Conference on Calorimetry in High Energy Physics, Tucson 1997, World Scientific, Singapore, 1998, pp. 182–193.
[6] N. Akchurin, et al., Nucl. Instr. and Meth. A 536 (2005) 29.
[7] N. Akchurin, et al., Nucl. Instr. and Meth. A 595 (2008) 359.
[8] N. Akchurin, et al., Nucl. Instr. and Meth. A 598 (2009) 710.
[9] B. Adeva, et al., Nucl. Instr. and Meth. A 289 (1990) 35.
[10] N. Akchurin, et al., Nucl. Instr. and Meth. A 584 (2008) 304.
[11] W.R. Nelson, H. Hirayama, D.W.O. Rogers, EGS4, SLAC Internal Report 165, Stanford Linear Accelerator Center, 1985.
[13] N. Akchurin, et al., Nucl. Instr. and Meth. A 598 (2009) 422.